HHS Public Access

Author manuscript

Neuroimage. Author manuscript; available in PMC 2020 October 01.

Published in final edited form as:

Neuroimage. 2020 October 01; 219: 116997. doi:10.1016/j.neuroimage.2020.116997.

Visualization of live, mammalian neurons during Kainate-infusion using magnetic resonance microscopy

Jeremy J. Flint[a,d,*], **Kannan Menon**[b,d], **Brian Hansen**[f], **John Forder**[b,c,d,g], **Stephen J. Blackband**[a,d,e,g]

[a]Department of Neuroscience, University of Florida, Gainesville, FL, USA

[b]Department of Biomedical Engineering, University of Florida, Gainesville, FL, USA

[c]Department of Radiology, University of Florida, Gainesville, FL, USA

[d]McKnight Brain Institute, University of Florida, Gainesville, FL, USA

[e]Center for Structural Biology, University of Florida, Gainesville, FL, USA

[f]Center of Functionally Integrative Neuroscience, Aarhus University, Denmark

[g]National High Magnetic Field Laboratory, Tallahassee, FL, USA

Abstract

Since its first description and development in the late 20th century, diffusion magnetic resonance imaging (dMRI) has proven useful in describing the microstructural details of biological tissues. Signal generated from the protons of water molecules undergoing Brownian motion produces contrast based on the varied diffusivity of tissue types. Images employing diffusion contrast were first used to describe the diffusion characteristics of tissues, later used to describe the fiber orientations of white matter through tractography, and most recently proposed as a functional contrast method capable of delineating neuronal firing in the active brain. Thanks to the molecular origins of its signal source, diffusion contrast is inherently useful at describing features of the microenvironment; however, limitations in achievable resolution in magnetic resonance imaging (MRI) scans precluded direct visualization of tissue microstructure for decades following MRI's inception as an imaging modality. Even after advancements in MRI hardware had permitted the visualization of mammalian cells, these specialized systems could only accommodate fixed specimens that prohibited the observation and characterization of physiological processes. The

[*]Corresponding author. Department of Neuroscience, 1149 Newell Drive, L1-100, University of Florida, Gainesville, FL, 32611, USA. jflint@mbi.ufl.edu (J.J. Flint).

Author contributions

JJF designed the study with BH advising on methodology. KM and JF assisted JJF with the development and application of the perfusion rig. JF and SJB advised on MRI studies and provided MRM expertise. JJF performed the MR and histological imaging. BH performed the MR data analysis. JJF and BH interpreted data. JJF wrote the manuscript. JJF and BH revised the manuscript. All authors contributed to final editing of the manuscript. JJF acquired funding for the study.

CRediT authorship contribution statement

Jeremy J. Flint: Conceptualization, Investigation, Methodology, Writing - original draft, Funding acquisition. **Kannan Menon:** Writing - review & editing. **Brian Hansen:** Methodology, Formal analysis, Writing - review & editing. **John Forder:** Writing - review & editing. **Stephen J. Blackband:** Resources, Writing - review & editing.

Appendix A. Supplementary data

Supplementary data to this article can be found online at https://doi.org/10.1016/j.neuroimage.2020.116997.

goal of the current study was to visualize cellular structure and investigate the subcellular origins of the functional diffusion contrast mechanism (DfMRI) in living, mammalian tissue explants. Using a combination of ultra-high field spectrometers, micro radio frequency (RF) coils, and an MRI-compatible superfusion device, we are able to report the first live, mammalian cells—α-motor neurons—visualized with magnetic resonance microscopy (MRM). We are also able to report changes in the apparent diffusion of the stratum oriens within the hippocampus—a layer comprised primarily of pyramidal cell axons and basal dendrites—and the spinal cord's ventral horn following exposure to kainate.

Keywords

Magnetic resonance microscopy; Acute slice; Kainate; α-motor; Hippocampus; Diffusion kurtosis

1. Introduction

The ability to use diffusive properties of water molecules as a contrast mechanism in MR imaging has enjoyed a thirty-year development history. Thanks to the length scales typically traversed by water molecules at physiological conditions, diffusion contrast is useful for probing the microscopic environment of biological tissues. Since its inception, diffusion weighted imaging has been used to quantify tissue diffusivity (Le Bihan et al., 1986), to reveal the three-dimensional orientation of white matter (Mori et al., 1999), and even touted alongside spectroscopic methods sensitive to sugar metabolism as one of the growing number of complimentary functional contrast mechanisms to blood-oxygen-level dependent (BOLD) based techniques (Le Bihan et al., 2006; Roussel et al., 2019).

Using ultra-high-field spectrometers as are commonly employed in the laboratory for analytical chemistry applications, it became possible to differentiate microscopic tissue structures with MRI at resolutions sufficient to visualize mammalian cells (Flint et al., 2009). When employing diffusion-based contrast mechanisms, even some subcellular components of the largest neurons—α-motors—could be differentiated from adjacent tissue types (Flint et al., 2012). These early studies were of interest primarily because they permitted direct observation and quantification of cellular-level tissue microstructure using MR. Prior to such improvements in MRI's resolution capacity, these properties could not be measured in cells and were only inferred through modeling analysis applied to macroscopic scan data. Despite offering an improved analysis capacity for tissue microstructure, the techniques employed for cellular resolution MR imaging studies were far from ideal for investigating mechanisms related to physiology. One such limitation includes difficulties inherent to conducting echo-planar imaging (EPI) at microscopic resolutions. Despite the fact that EPI techniques offer imaging times on the order of seconds making them an obvious choice for studying dynamic changes in living tissues, complications arise when using this method for MR microscopy studies. So-called off-resonance effects result from heightened susceptibility, sensitivity to B_0 field inhomogeneities, and eddy currents generated by field gradients (Chung et al., 2011; Alexandra and Allan, 2012; Oh et al., 2012; Ciobanu, 2017). These effects become worse as the magnetic field strength increases and manifest as geometric distortions in the acquired image. Also of note, the lack of MR-

compatible, metabolic support devices for live, excised mammalian samples precluded their use in cellular-level MR microscopy studies and thus necessitated employing fixed histological specimens or cells from hypoxia-resistant aquatic models (Hsu et al., 1996). Given these limitations, methods used in the earliest magnetic resonance microscopy (MRM) studies on cells generally included long imaging times and often suffered from aldehyde fixation as a confounding factor (Aguayo et al., 1986; Ciobanu et al., 2003; Ciobanu and Pennington, 2004; Flint et al., 2009).

In previous publications, we have described a device designed and built for conducting MR microscopy studies on living tissue samples (Flint et al., 2015, 2017). This equipment was designed to operate within a functioning spectrometer during data collection while maintaining the viability of an excised tissue sample through superfusion: the continuous passage of oxygenated, nutrient rich media over the tissue's exterior. In the current study, we present the first instance of diffusion-weighted MR images capturing live mammalian neurons: the perikarya and primary neurites of rat α-motors located in the lumbar enlargement. In addition, we perform kainate exposure studies (100 μM kainate) *in situ* on ventral horn regions containing α-motor neurons as well as the pyramidal cells in the CA1 region of the rat hippocampus. While both regions are comprised of central nervous system (CNS) tissues, the distinct morphologies of the ventral horn and CA1 region lend complimentary features to the current study. The subcellular features of pyramidal neurons in the hippocampus' CA1 region are divided by and concentrated within specific hippocampal laminae such that each distinguishable layer only contains specific, subcellular elements of the neurons: oriens = pyramidal axons & basal dendrites, pyramidale = cell bodies, radiatum = apical dendrites. In this way, we can investigate their individual contributions to diffusion-based signal changes following kainate exposure despite our inability to visualize these components directly. Likewise, the ventral horn of the spinal cord contains large, discrete cell bodies of α-motor neurons. While these cells are not as resistant to the detrimental effects of kainate exposure—which causes tonic firing patterns in neuronal populations ultimately leading to excitotoxic death—their morphological and contrast characteristics allow them to be visualized individually on a cell-by-cell basis.

2. Methods

2.1. Superfusion rig preparation

To prepare the apparatus for a fresh tissue sample and to prevent residual contamination of kainate in the superfusion rig between samples, we began each experiment by flushing any remaining volume of superfusate from the device using air. Next, RO water was pumped into the emptied rig at a rate of 2 ml/min overnight for a period between 12 h and 18 h. Following this wash step, the rig was emptied again using air and then primed with fresh, artificial cerebrospinal fluid (aCSF)—120 mM NaCl, 26 mM $NaHCO_3$, 10 mM $C_6H_{12}O_6$, 3 mM KCl, 2 mM $CaCl{\bullet}H_2O$, 1.5 mM KH_2PO_4, 1.4 mM $MgSO_4{\bullet}7H_2O$)—bubbled with carbogen (95% O_2, 5% CO_2). Priming with aCSF continued for 3h at a rate of 2 ml/min prior to the introduction of a freshly prepared, acute tissue slice.

2.2. Acute slice preparation

All animal experiments described conformed to federal guidelines set forth in the *Guide for the Care and Use of Laboratory Animals* and were reviewed and approved by the University of Florida Institutional Animal Care and Use Committee (IACUC). Sprague Dawley rats (≥350 g) were anesthetized by inhalation of 4% isoflurane in an oxygen carrier gas at a flow rate of 2L/min for 4min. Lack of righting, toe-pinch, and ocular reflexes were confirmed in the unconscious animals immediately prior to euthanasia by guillotine decapitation. The whole brain or lumbar spinal cord enlargement was then isolated by gross dissection. For acute hippocampal slice preparations, the portion of the brain containing the hippocampus—rostral to the cerebellum and caudal to the olfactory bulbs—was removed and placed into a vibratome cutting bath using cyanoacrylate glue. In the case of acute slices from the spinal cord, a 4 mm long segment was embedded in ultra-low gelling temperature agarose gel (A2576, Millipore Sigma) prior to slicing as part of a modified protocol based on previously described methods (Carp et al., 2008; Mitra and Brownstone, 2012). The gel was prepared at a concentration of 4% using carbogen (95% O_2, 5% CO_2) bubbled aCSF as a solvent. Spinal cord segments were placed in 15 x 15 × 5 mm polyvinyl chloride molds (27183, Ted Pella) containing agarose gel and snap-cooled in a 4 °C refrigerator (2min) prior to adhesion in the cutting bath with cyanoacrylate glue. Acute hippocampal (300 μm) and spinal cord (200 μm) slices were prepared in an ice-cold vibratome bath containing aCSF continuously bubbled with carbogen (95% O_2, 5% CO_2).

2.3. dMRI of live α-motor neurons

MR microscopy studies were performed on a 600 MHz Oxford spectrometer interfaced with an Avance III Bruker console. Acute, transverse slices (200 μm) from the lumbar enlargements of rat spinal cords (n = 2) were prepared as described above. Slices were placed in a modified, 200 μm diameter micro surface-coil (B6371/0001, Bruker Biospin) (Fig. 1) and interfaced with our MR-compatible superfusion equipment.

All MR imaging conducted as part of the current study was performed using traditional, pulsed gradient spin echo (PGSE) acquisition implemented in a conventional, spin-warp (i.e. non-EPI) sequence with full sampling: no acceleration via partial Fourier acquisition, etc. Continuous superfusion with aCSF (2 ml/min, 23° C) was applied while diffusion-weighted, 3D images (TE/TR = 13/2000 ms, b effective = 1900 s/mm^2, Δ = 6.5 ms, δ = 1.2 ms, Matrix = 128 isotropic, FOV = 1.39 mm isotropic, 11 μm isotropic resolution, Acquisition Bandwidth = 50,000 Hz, NEX = 1, Time = 9 h 6 min) or (TE/TR = 13/2000 ms, b effective = 1900 s/mm^2, Δ = 6.5 ms, δ = 1.2 ms, Matrix = 128 x 128 x 32, FOV = 1.39 x 1.39 × 0.35 mm, 11 μm isotropic resolution, Acquisition Bandwidth = 50,000 Hz, NEX = 1, Time = 2 h 16 min) were collected.

2.4. Diffusion-weighted imaging in α-motor and CA1 pyramidal neurons after kainate exposure

Acute hippocampal (300 μm, n = 8) or spinal cord (200 μm, n = 5) slices were prepared and loaded into the superfusion rig as previously described (Fig. 2).

Note that the spinal cord slices employed in our kainate exposure study were different samples than those used for our 3D collections described in section 2.3. Typical slice preparation times—from euthanasia to superfusion—were 50 min and 115 min respectively with the spinal cord slices taking more time to prepare due to the additional agarose embedding procedure. In order to ensure consistently high sample quality, brain slice preparation times in excess of 1 h 30 min were pre-established as exclusion criteria because short post-mortem intervals are known to increase tissue viability and signal stability. Although care was taken to ensure optimal tissue conditions and prolong slice viability, inherent limitations of the acute slice model include a constant state of sample deterioration that becomes worse over time. Our control experiments tracking the rate of diffusion signal change in this model evidenced a relatively stable tissue microenvironment over the time intervals being employed which were typical of well-maintained, acute slice preparations; however, this metric should not be taken to mean that our samples were somehow impervious to the dynamic changes that inevitably take place in all acute slice preparations (Flint et al., 2015). Kainate exposure studies were performed under constant temperature (23° C) and continuous flow (2 ml/min) of aCSF superfusate. For pyramidal cell studies, diffusion weighted series (TE/TR = 13/2000 ms, b effective = 600, 700, 800, 1300, 2000, 3600, and 4800 s/mm^2, δ = 1.2 ms, Δ = 6.5 ms, res = 16 × 16 μm in-plane, 200 μm thick image slice, Acquisition Bandwidth = 50,000 Hz, NEX = 4, time = 8.5 min per scan: 59.5 min total) were collected to establish baseline diffusion signal properties in the CA1 region. In addition, four stability control scans were conducted at the end of the series with one—a temporal control—being a duplicate of the first scan in the experimental series (b effective = 600 s/mm^2) and the remaining three—directional controls—being duplicates of the second scan in the experimental series albeit with variable diffusion gradient directions (b effective = 700 s/mm^2, x,y,z = 1,0,0; 0,1,0; 0,0,1). Next, the slices were exposed to aCSF superfusate (2 ml/min) containing 100 μM kainate (K0250, Millipore Sigma) for 30 min. Following this exposure to kainate, an identical, diffusion weighted, experimental image series was collected while the exposure to kainate-spiked aCSF (100 μM kainate, 2 ml/min) continued. Lastly, following the kainate exposure series, an additional, temporal control scan (b effective = 600 s/mm^2) was collected. Total imaging time for a hippocampal slice experiment was 3 h 12 min. For α-motor neuron activation studies, a four-scan, diffusion weighted image series (TE/TR = 13/2000 ms, b effective = 1200, 1500, 2300, 3800 s/mm^2, δ = 1.2 ms, Δ = 6.5 ms, res = 8.9 μm in-plane, 200 μm thick image slice, NEX = 4, time = 17 min per scan: 68 min total) was collected to establish the baseline diffusion properties in the 200 μm thick transverse slice from the lumbar enlargement. Next, the slices were exposed to aCSF superfusate (2 ml/min) containing 100 μM kainate for 30 min. Finally, an additional four-scan, diffusion weighted image series was collected while the exposure to kainate-spiked aCSF (100 μM kainate, 2 ml/min) continued. Total imaging time for a spinal cord slice experiment was 2 h 46 min. To compare the pre- and post-exposure states in the tissues tested, diffusion signal was quantified at each b value collected from regions of interest (ROIs) drawn in the strata oriens, pyramidale, and radiatum (hippocampus) or across the gray matter tissue—whole coil field of view—of the ventral horn (spinal cord).

In this analysis, we account for the observed non-mono-exponential signal decay by employing the diffusion kurtosis imaging (DKI) framework (Jensen et al., 2005). As our

data are single direction acquisitions, we estimate only apparent kurtosis and apparent diffusivity by fitting log-normalized ROI average signals to:

$$\log S(b,\hat{n}) = -bD(\hat{n}) + \frac{1}{6}b^2 D(\hat{n})^2 K(\hat{n}) \quad (1)$$

where b is diffusion weighting, $D(\hat{n})$ and $K(\hat{n})$ are the apparent diffusivity and kurtosis, respectively, observed along the diffusion encoding direction $\hat{n}$. Fitting was performed in Matlab (The Mathworks inc.) using nonlinear optimization as in (Kjølby et al., 2016). For each tissue type, the group means of $D(\hat{n})$ and $K(\hat{n})$ for both the pre and post exposure states were compared using a two-tailed, paired Student's t-test.

3. Results

3.1. dMRI of live α-motor neurons

MR microscopy experiments (n = 2, 11 μm isotropic resolution) collected in acute slice preparations (200 μm thick) taken from the lumbar enlargement in rats yielded 3D images containing multiple cell bodies of α-motor neurons (Fig. 3).

Regions of the diffusion-weighted scans containing intracellular space exclusively—i.e. the cell bodies of the α-motors—present with hypointense signal as opposed to the remaining gray matter of the ventral horn that appears bright by comparison. Such characteristics denote higher diffusivity within perikarya of α-motors relative to the tissues of the neuropil that surround them.

3.2. Diffusion-weighted imaging in α-motor and CA1 pyramidal neurons after kainate exposure

In the hippocampal lamina measured before and after exposure to kainate, the stratum oriens exhibited significant changes in its apparent diffusion coefficient ($D(\hat{n})$, or ADC) (Fig. 4).

Using a two-tailed, paired Student's t-test with an α value of 0.05, the p-value calculated for the oriens was 0.045. Interestingly, the observed changes in ADC were opposite in magnitude becoming greater in the stratum oriens and smaller in the stratum radiatum (Table 1). The strata pyramidale and radiatum did not exhibit significant changes to their ADCs in response to kainate exposure. Control scans (b effective = 600 s/mm^2) testing for diffusion signal stability over the time courses of the pre and post exposure imaging intervals (68 min per interval) exhibited a rate of signal change less than or equal to the expected change quantified in the acute slice model: expected signal change over 68 min interval = 0.658 %; observed signal change in the 68 min interval pre kainate = 0.424 %; observed signal change in the 68 min interval post kainate = 0.562 %. Control scans employing variable diffusion gradient directions (b effective = 700 s/mm^2, x,y,z = 1,0,0; 0,1,0; 0,0,1) exhibited diffusion signal equivalency within each tissue group: p-values = 0.15 to 0.93. These results confirmed the lack of effect of tissue orientation on diffusion signal in our model and justified use of a single orientation diffusion gradient in our image collections (see also discussion section 4.2). Equivalent statistical testing in the spinal cord samples revealed significant changes to the ADC following exposure to kainate: p-value = 0.042. This

activation based change resulted in a decrease of ADC following exposure to kainate. None of the tissues tested exhibited significant changes in apparent kurtosis following chemical activation (Table 1).

4. Discussion

4.1. Diffusion MRI of live α-motor neurons and CA1 pyramidal cells

The diffusion-weighted MR microscopy data of α-motor and pyramidal neurons presented in the current manuscript are the first reported instance of live, mammalian cells visualized directly using MR techniques. While the finest details of tissue microstructure may be lacking in these images, the inherent contrast generated between the cell bodies and primary neurites of α-motors and the adjacent parenchymal tissues of the ventral horn does reveal important and heretofore unknown qualities about the intrinsic diffusion properties of subcellular elements within the microenvironment of live tissues. First, it shows that the apparent diffusivity within the cell bodies of α-motor neurons is far greater than that of the ventral horn tissue surrounding them. This finding refutes the typical assumption of low intracellular diffusivity often attributed to cellular organelles or cytoplasmic components acting as physical barriers to water diffusion: that is, at least for cases employing diffusion times similar to those used here (Goodsell, 1991; Fulton, 1982; Stanisz, 2003). Second, the preservation of these diffusion contrast characteristics between this study and previous works using aldehyde-fixed tissue samples reveals that the high intracellular apparent diffusivity observed does not result from fixation-based changes in membrane permeability. Lastly, because the hippocampal laminae consisting of cell bodies (stratum pyramidale) and their projections (strata oriens and radiatum) express equivalent diffusion contrast characteristics to the cell bodies of α-motor neurons and the ventral horn tissues which surround them respectively, it shows that these distinctive diffusion characteristics are preserved across neuronal subtypes. While it would be presumptuous to assume that the diffusion properties described apply to all mammalian cell types—or even neuronal types for that matter—our data do show that high diffusivity in tissue regions comprised of cell bodies and low diffusivity in tissue regions comprised of cellular extremities are characteristics shared by two distinct neuronal populations with vastly different physiological and morphological characteristcs.

4.2. On the use of unidirectional diffusion encoding

A serious experimental challenge faced in the design of our study is the conflict between the acute slice model's need for relatively short scan times (even with our superfusion setup) and the rather long scan times needed for cellular resolution MRM with sufficient signal to noise ratio (SNR) for quantitative analysis. As accelerating acquisitions by the use of EPI seems untenable with the microcoil setup employed here, we are left with the option to reduce scan time by reducing the number of diffusion encodings. At the same time, we wanted to employ the DKI framework because of its proven sensitivity to microstructure with clinical applicability but also because of its virtues as a model-free analysis framework (Hansen and Jespersen, 2017). Generally, enough encoding directions should be acquired to estimate rotationally invariant metrics such as mean diffusivity and a mean kurtosis. The exception to this is when tissues are isotropic in which case the apparent diffusivity and

kurtosis will be equal to their directional averages. Previous MRM studies of the hippocampus have found very low anisotropy in the hippocampal (HC) subfields we set out to explore (Shepherd et al., 2007). Based on this experimental evidence (Shepherd et al., 2007) which is supported by modeling studies (Hansen and Jespersen, 2016; Schilling et al., 2017) and known HC histology, we decided to design our experimental protocol so that a unidirectional data set allowing estimation of apparent diffusivity and kurtosis could be acquired in a time window characterized by relatively stable slice conditions. Although not rotationally invariant, the low anisotropy reported in the strata oriens (SO) and radiatum (SR) in (Shepherd et al., 2007) indicates that these measures are reasonable surrogates for the mean diffusivity (MD) and mean kurtosis (MK) for our purposes. However, to confirm that these conditions applied to our model system, we included control scans collected at three orthogonal directions between the pre and post exposure acquisition series. As expected, these measurements confirmed that negligible directional signal variation is detected and that, in our case, data based on unidirectional measurements are adequate. If one were to speculate about the cause of the low anisotropy in these HC regions, much can be learned from the study by Shepherd et al. (2007). In their study, diffusion tensor microscopy was used to evaluate diffusion and anisotropy properties in formalin fixed, *ex vivo* human hippocampus. Here, the anisotropy was seen to be highest in the fimbria—a densely knit bundle of highly myelinated white matter—which was the only hippocampal subregion to register an FA significantly different from the rest of the laminae (Shepherd et al., 2007). The other HC regions also exhibited similar diffusivities. Notably, they found that the strata oriens and radiatum have similar fractional anisotropy (FA) values—on the order of 0.15–0.3 respectively. These low FA values were argued to stem from the complexity of these tissues where multiple fiber connections cross. So, while these regions do contain cells with well-ordered projections, these coexist with other fiber orientations to an extent where FA becomes surprisingly low. The same collapse of FA in complex tissue arrangements was previously described and explored both experimentally and with numerical simulations (Hansen and Jespersen, 2016).

The study by Shepherd et al. (2007) used 300 μm thick slices and 60 μm in-plane resolution: significantly lower than the 16 μm^2 in-plane resolution reported currently. One might therefore expect to see less partial volume effects in our data based on the assumption that, at the reported resolutions, each voxel will contain only one dominant fiber direction. This would lead to strong signal variation with changing gradient direction which again is the opposite of what we report in our results. The explanation for this might be gleaned from a recent study by Schilling et al. (2017) where the effect of spatial resolution on the crossing fiber problem in white matter was investigated. Surprisingly, that study found the amount of fiber crossings actually increases with increasing spatial resolution, and this phenomenon was reported in the relatively well-ordered white matter. We think it likely that the same effect exists in the hippocampal laminae examined here which, in our case, are tissues comprised almost entirely of gray matter but also containing sparse, myelinated fibers.

4.3. Diffusion-weighted imaging in CA1 pyramidal neurons and the lumbar enlargement's ventral horn following kainate exposure

Diffusion weighted MRM in the CA1 region of the rat hippocampus paired with superfusion techniques revealed variations in the laminar response to kainate exposure. When diffusion properties of tissues were compared before and after kainate treatment (100 μM), apparent diffusivity increased in the stratum oriens (13.7%), decreased in the stratum radiatum (9.5%), and increased in the stratum pyramidale (7.3%). Importantly, only the observed change in the stratum oriens was shown to be statistically significant ($p = 0.045$) while the changes in the stratum radiatum ($p = 0.076$) and pyramidale ($p = 0.081$) were not. The opposing changes in apparent diffusivity between the strata oriens and radiatum upon activation with kainate was an interesting and unexpected result. One recent compartmental modeling study has estimated intra-axonal diffusivity to be roughly four times higher than extra-axonal diffusivity in the genu of the rat (Kunz et al., 2018). It seems likely then that the primary axon of pyramidal cells is also a tissue region of relatively high diffusivity. Moreover, this structure shares a tissue compartment with the perikaryon where we have consistenly observed high diffusivity conditions. In this scenerio, water intake associated with action potential propagation could explain our observation of an increase in apparent diffusivity within the stratum oriens upon kainate exposure (Teorell, 1962; Iwasa et al., 1980; Tasaki and Iwasa, 1981; Kim et al., 2007). Following from this, the reason a similar increase was not observed in the stratum radiatum could be attributed to the loss of afferent signaling from—and subsequent loss of water uptake into the axons of—Schaffer collaterals.

Multiple studies investigating both activity dependent and hypotonic-stress based cell swelling in the excised buccal ganglia of Aplysia californica have reported results describing both volume and ADC increases within perikarya occuring concomitantly with ADC decreases in the ganglia containing these same cell bodies (Jelescu et al., 2014; Abe et al., 2017). These results are interesting from a biological point of view but physically it is not surprising that the overall diffusion properties of a tissue can differ from those of individual subcompartments within the tissue. Our findings are in agreement with the reports doumented in aplysia except that here we cannot resolve individual neurons residing in the hippocampus (Jelescu et al., 2014; Abe et al., 2017). Given the similarity of our results, it's plausible that diffusivity changes in the strata oriens or radiatum could oppose those observed within neurons comprising these same tissues via some as of yet unknown or mis-attributed mechanism of water behavior occuring at the microstructural level: such as diffusivity changes in adjacent, non-neuronal cell populations. Our study relies on chemically induced tissue perturbation with kainate, and any such design must acknowledge its toxic properties. This is particularly important for diffusion based investigations where the effects on diffusion are impossible to disambiguate from those of chemically induced activation. Nevertheless, we attempted to mitigate these potential confounds by selecting a cell population—the CA1 pyramidal neurons—with an increased resistance to kainate's excitotoxic effects. Furthermore, if our results were the effect of excitotoxic edema, we would not expect to see the regionally different tissue responses reported. Acute ischemia is known to produce only diffusivity decreases, and these would presumably occur throughout our slice in response to kainate poisoning. Stronger evidence for the soundness of our approach might be abtained in future studies by employing additional metrics of function—

such as electrophysiology recordings—and tests for viability—such as flourescent dye exclusion experiments—in order to better isolate the root causes of the effects of kainate exposure.

When comparing raw diffusion signal change in the kainate treated hippocampus, values expressed between pre- and post-exposure states in individual laminae (+3.7% [radiatum]; −8.6% [oriens]) were notably smaller in magnitude—and, in the case of the stratum oriens, opposite in sign—to those measured in similar, albeit lower resolution studies of the entire CA1 region conducted previously in our multi-slice perfusion apparatus (+18%) (Flint et al., 2009). There are many factors which could potentially contribute to the discrepancies in quantified diffusion changes—both magnitude and sign—between the two studies. Concerning the differences in magnitude, one key change in our methodology was the switch to the continuous flow, in-bore oxygenator hardware (Flint et al., 2015). This device provides a steady exchange of superfusate which ensures a constant supply of metabolites as well as continuous removal of metabolic waste products. Thus, improvements in the tissue environment as evidenced by the increased diffusion signal stability reported in (Flint et al., 2015) is likely responsible for the reduction in magnitude of kainate-induced diffusion signal change compared to previous studies (Flint et al., 2009).

When comparing the results from our 2009 study to the present findings, one also has to take into account differences in the slice preparation. Excision of the CA3 region was necessitated in the current study due to space limitations inside the microperfusion well, but was not required in the multislice perfusion apparatus employed in our 2009 study. While we believe our slice preparation is functional (as argued above) we cannot ignore the fact that ablation of the CA3 region reduces pyramidal neuron firing due to the loss of excitatiory, gultamatergic input to the CA1 pyramidal cells through Schaffer collaterals. Previous studies have reported a reduction in spontaneous excitatory post synaptic currents (EPSCs) from CA1 pyramidal neurons of 20% following removal of the tissues within CA3 (Banerjee et al., 2013). Thus, given that CA3 ablation results in a significant reduction in EPSCs, the possibility that this reduction would lead to a decrease in cell firing—and, subsequently, a decrease in magnitude of activation-based diffusion signal change-—seems feasible. However, due to the similarities in action between Schaffer collaterals and kainate —both act on the excitatiory, glutamatergic AMPA receptors of CA1 pyramidal neurons— any reduction in pyramidal cell firing attributable to the removal of input from CA3 would almost surely be reversed by the presently described bath application of 100 μM kainate (Hampson et al., 1992). We therefore attribute the lower signal modulation amplitude primarily to improvements in the superfusion setup while ackowledging more research into the compartmental nature of diffusivity at the cellular level is waranted.

As for the apparent discrepancy in response to diffusivity changes within the stratum oriens when compared to our 2009 activation study, this seemingly bizarre reversal in diffusion properties can be accounted for by considering the effects of volume averaging. A related effect—as discussed above—was reported in Aplysia californica ganglia where both volume and ADC increases within perikarya were observed to occur simultaneaously with ADC decreases in the ganglia as a whole (Jelescu et al., 2014; Abe et al., 2017). We believe a similar resolution effect can explan this phenomenon considering the highly volume

averaged, relatively low resolution MRM data collected in (Flint et al., 2009) as contrasted with the far less volume averaged, high resolution data from our present study. Limitations of our previous collections which were taken at lower resolution and with a less than ideal tissue maintenance regimen can account for the differences in results between studies and highlights the importance of improved tissue discrimination and treatment in the current study.

While laminae with larger physical dimensions were readily discernible in our hippocampal perturbation experiments, cell bodies of α-motor neurons were not and thus had to be included as an amalgamated whole—inclusive of all gray matter tissue within the ventral horn—when quantifying diffusion changes. Kainate driven diffusivity changes in the spinal cord's ventral horn resulted in a 23.9 % decrease in apparent diffusivity. This response is akin to that observed in the stratum radiatum as kainate exposure resulted in a decrease in ADC in both tissues. Given the higher proportion of neuropil—as opposed to cell bodies—in the ventral horn, it is possible that the microstructural origins of the ADC decrease reside in the tissue regions surrounding the α-motor perikarya. While it is tempting to draw such comparisons given the similarities in microstructural content—dendritic arbors, axons, extracellular matrix, astrocytes, microvasculature, etc.—and ADC response, further studies are needed to confirm the true microstructural origins of this ADC change.

The DKI framework was employed in this study as a means of summarizing the signal curves via two basic parameters: namely the apparent diffusivity ($D(\hat{n})$) and the apparent kurtosis ($K(\hat{n})$). Including the kurtosis term—which accounts for deviations from Gaussian diffusion—has been shown to improve diffusivity estimates (Veraart et al., 2011). Preprocessing with denoising as in (Hansen et al., 2017) was tested but did not affect results (Supplementary Fig. 1), and this step was ultimately abandoned in favor of employing minimally processed data in our analysis. While our results indicate diffusivity changes upon exposure to kainate, apparent kurtosis values did not differ significantly between the pre and post treatment states. This is surprising given that DKI is known to offer improved microstructural sensitivity over conventional diffusion tensor imaging (DTI) (Hansen and Jespersen, 2017). One could speculate that protocols with more diffusion encoding directions might produce more robust (i.e. less influenced by noise and rotationally invariant) kurtosis metrics (e.g., the mean kurtosis) capable of revealing subtle, activation-driven microstructural modulations. Fast diffusion kurtosis methods—which are also compatible with more detailed white matter modeling approaches—might be feasible as compact DKI implementations for MR microscopy (Hansen et al., 2016, 2017). Such methods require fewer encoding directions than those utilized in previous, cellular-level diffusion tensor tractography (DTT) studies and might be suitable for future MRM studies of live slices (Flint et al., 2010; Hansen et al., 2011). Despite the odd absence of significant, activation-induced changes in kurtosis, our findings are nevertheless plausible in that ADC changes have also been observed as an early marker of learning induced plasticity (Blumenfeld-Katzir et al., 2011). Despite such findings and the widespread clinical use of ADC changes for stroke diagnosis, interpretation of these ADC changes in terms of distinct cellular features or events remains elusive. Nevertheless, our results are in keeping with such DWI findings in that ADC here seems to reflect tissue changes at the cellular level (although

not in the soma-rich stratum pyramidale) that occur over relatively short time scales: in our case, minutes after kainate exposure.

4.4. Regarding a water-based functional contrast mechanism

A functional contrast mechanism dependent on water diffusivity (DfMRI) promised to offer a far more direct means to detect neuronal firing than similar blood-oxygen-level-dependent (BOLD) based methodology. While initial reports fueled interest for and debate over the possibility of such a mechanism in mammals, subsequent findings linking the observed, function-based diffusivity changes to cell swelling began to cast doubt on the utility of DfMRI contrast to detect normal, non-pathological neural function (Jelescu et al., 2014; Abe et al., 2017). Recently, one such study confirmed the lack of diffusion response during periods of natural, spontaneous neuronal depolarization in organotypic cortical slices (Bai et al., 2016). In light of such findings, the possibility of attaining a functional contrast mechanism based on water diffusion for practical use in the clinic seems all but lost.

While diffusivity may not be the mechanism by which we achieve functional detection at the cellular level, other methods based on water dynamics occurring at the microstructural level may still offer such a possibility. Recent studies by Springer Jr. and Bai et al. describe a measurement technique to detect active, transmembrane water cycling (AWC) which correlates with neuronal activity (Bai et al., 2018; Springer, 2018). Zhang et al. first described this active water transport mechanism in an NMR investigation involving suspensions of yeast cells (Zhang et al., 2011). While this particular mechanism still presents with serious practical limitations—primarily the reliance on blood-brain-barrier impermeable contrast agents—the ability to detect such functionally dependent water dynamics represents a huge step towards attaining a functional MR contrast mechanism linked directly to neuronal firing. Given what we understand about the microstructural origins of MR contrast, it is not hard to imagine a future in which water cycling could comprise the biological mechanism for a new method of functional imaging while diffusion contrast could be employed in new techniques used to identify pre-pathological neuronal populations in the earliest stages of cytotoxic edema when they are still amenable to treatment interventions.

Supplementary Material

Refer to Web version on PubMed Central for supplementary material.

Acknowledgements

Funding provided by the National Institute of Neurological Disorders and Stroke of the National Institutes of Health [grant number R21NS094061]; MR imaging studies were performed in the McKnight Brain Institute at the National High Magnetic Field Laboratory's AMRIS Facility, which is supported by the National Science Foundation [Cooperative Agreement Nos. DMR-1157490 and DMR-1644779]; Light microscopy images were collected in the McKnight Brain Institute's Cell and Tissue analysis Core CTAC facility.

References

Abe Y, Nguyen KV, Tsurugizawa T, Ciobanu L, Le Bihan D, 2017 Modulation of water diffusion by activation-induced neural cell swelling in Aplysia Californica [sic]. Sci. Rep 7, 6178 10.1038/s41598-017-05586-5. [PubMed: 28733682]

Aguayo JB, Blackband SJ, Schoeniger J, Mattingly MA, Hintermann M, 1986 Nuclear magnetic resonance imaging of a single cell. Nature 322, 190–191. 10.1038/322190a0. [PubMed: 3724861]

Alexandra B, Allan JG, 2012 Magnetic resonance microscopy. Anal. Cell Pathol. 35 (4), 205–277. 10.3233/ACP-2011-0050.

Bai R, Stewart CV, Plenz D, Basser PJ, 2016 Assessing the sensitivity of diffusion MRI to detect neuronal activity directly. Proc. Natl. Acad. Sci. Unit. States Am. E1728–E1737. 10.1073/pnas.1519890113.

Bai R, Springer CS Jr., Plenz D, Basser PJ, 2018 Brain active transmembrane water cycling measured by MR is associated with neuronal activity. Magn. Reson. Med 1–16. 10.1002/mrm.27473.

Banerjee J, Alkondon M, Albuquerque EX, Pereira EFR, 2013 Contribution of CA3 and CA1 pyramidal neurons to the tonic α7 nAChR-dependent glutamatergic input to CA1 pyramidal neurons. Neurosci. Lett 554, 167–171. [PubMed: 23973303]

Blumenfeld-Katzir T, Pasternak O, Dagan M, Assaf Y, 2011 Diffusion MRI of structural brain plasticity induced by a learning and memory task. PloS One 6 (6). 10.1371/journal.pone.0020678 e20678. [PubMed: 21701690]

Carp JS, Tennissen AM, Mongeluzi DL, Dudek CJ, Chen XY, Wolpaw JR, 2008 An *in vivo* protocol for recording from spinal motoneurons of adult rats. J. Neurophysiol 100, 474–481. 10.1152/jn.90422.2008. [PubMed: 18463177]

Chung J-Y, In M-H, Oh S-H, Zaitsev M, Speck O, Cho Z-H, 2011 An improved PSF mapping method for EPI distortion correction in human brain at ultra high field (7T). Magn. Reson. Mater. Phy 24, 179–190. 10.1007/s10334-011-0251-1.

Ciobanu L, 2017 Hybrid pulse sequences In: Microscopic Magnetic Resonance Imaging: A Practical Perspective. CRC Press.

Ciobanu L, Pennington CH, 2004 3D micron-scale MRI of single biological cells. Solid State Nucl. Mag. 25, 138–141. 10.1016/j.ssnmr.2003.03.08.

Ciobanu L, Webb AG, Pennington CH, 2003 Magnetic resonance imaging of biological cells. Prog. Nucl. Magn. Reson. Spectrosc 42, 69–93. 10.1016/S0079-6565(03)00004-9.

Flint JJ, Lee C-H, Hansen B, Fey M, Schmidig D, Bui JD, King MA, Vestergaard-Poulsen P, Blackband SJ, 2009 Magnetic resonance microscopy of mammalian neurons. Neuroimage 46 (4), 1037–1040. 10.1016/j.neuroimage.2009.03.009. [PubMed: 19286461]

Flint JJ, Hansen B, Fey M, Schmidig D, King MA, Vetergaard-Poulsen P, Blackband SJ, 2010 Cellular-level diffusion tensor microscopy and fiber tracking in mammalian nervous tissue with direct histological correlation. Neuroimage 52 (2), 556–561. 10.1016/j.neuroimage.2010.04.031. [PubMed: 20403443]

Flint JJ, Hansen B, Portnoy S, Lee C-H, King MA, Fey M, Vincent F, Stanisz GJ, Vestergaard-Poulsen P, Blackband SJ, 2012 Magnetic resonance microscopy of human and porcine neurons and cellular processes. Neuroimage 60 (2), 1404–1411. 10.1016/j.neuroimage.2012.01.050. [PubMed: 22281672]

Flint JJ, Menon K, Hansen B, Forder J, Blackband SJ, 2015 A microperfusion and in-bore oxygenator system designed for magnetic resonance microscopy studies on living tissue explants. Sci. Rep. 5, 18095 10.1038/srep18095. [PubMed: 26666980]

Flint JJ, Menon K, Hansen B, Forder J, Blackband SJ, 2017 Metabolic support of excised, living brain tissues during magnetic resonance microscopy acquisition. JoVE 128 10.3791/56282 E56282

Fulton AB, 1982 How crowded is the cytoplasm? Cell 30 (2), 345–347. 10.1016/0092-8674(82)90231-8. [PubMed: 6754085]

Goodsell DS, 1991 Inside a living cell. Trends Biochem. Sci. 16, 203–206. 10.1016/0968-0004(91)90083-8. [PubMed: 1891800]

Hampson DR, Huang XP, Oberdorfer MD, Goh JW, Auyeung A, Wenthold RJ, 1992 Localization of ampa receptors in the hippocampus and cerebellum of the rat using anti-receptor monoclonal antibody. Neuroscience 50 (1), 11–22. 10.1016/0306-4522(92)90378-f. [PubMed: 1328932]

Hansen B, Jespersen SN, 2016 Kurtosis fractional anisotropy: its contrast and estimation by proxy. Sci. Rep 6, 23999 10.1038/srep23999. [PubMed: 27041679]

Hansen B, Jespersen SN, 2017 Recent developments in fast kurtosis imaging. Front. Physiol 5 10.3389/fphy.2017.00040.

Hansen B, Flint JJ, Heon-Lee C, Fey M, Vincent F, King MA, Vetergaard-Poulsen P, Blackband SJ, 2011 Diffusion tensor microscopy in human nervous tissue with quantitative correlation based on direct histological comparison. Neuroimage 57 (4), 1458–1465. 10.1016/j.neuroimage.2011.04.052. [PubMed: 21575730]

Hansen B, Lund TE, Sangill R, Stubbe E, Finsterbusch J, Jespersen SN, 2016 Experimental considerations for fast kurtosis imaging. Magn. Reson. Med 76 (5), 1455–1468. 10.1002/mrm.26055. [PubMed: 26608731]

Hansen B, Kahn AR, Shemesh N, Lund TE, Sangill R, Eskildsen SF, Østergaard L, Jespersen SN, 2017 White matter biomarkers from fast protocols using axially symmetric diffusion kurtosis imaging. NMR Biomed. 30 (9), e3741 10.1002/nbm.3741.

Hsu EW, Aiken NR, Blackband SJ, 1996 Nuclear magnetic resonance microscopy of single neurons under hypotonic perturbation. Am. J. Physiol 271, C1895–C1900. 10.1152/ajpcell.1996.271.6.C1895, 6 pt. 1. [PubMed: 8997190]

Iwasa KH, Tasaki I, Gibbons RC, 1980 Swelling of nerve fibers associated with action potentials. Science 210 (4467), 338–339. 10.1126/science.7423196. [PubMed: 7423196]

Jelescu IO, Ciobanu L, Geffroy F, Marquet P, Le Bihan D, 2014 Effects of hypotonic stress and ouabain on the apparent diffusion coefficient of water at cellular and tissue levels in Aplysia. NMR Biomed. 27, 280–290. 10.1002/nbm.3061. [PubMed: 24403001]

Jensen JH, Helpern JA, Ramani A, Lu H, Kaczynski K, 2005 Diffusional kurtosis imaging: the quantification of non-Gaussian water diffusion by means of magnetic resonance imaging. Magn. Reson. Med 53 (6), 1432–1440. 10.1002/mrm.20508. [PubMed: 15906300]

Kim GH, Kosterin P, Obaid AL, Salzberg BM, 2007 A mechanical spike accompanies the action potential in mammalian nerve terminals. Biophys. J 92 (9), 3122–3129. 10.1529/biophysj.106.103754. [PubMed: 17307820]

Kjølby BF, Khan AR, Chuhutin A, Pedersen L, Jensen JB, Jakobsen S, Zeidler D, Sangill R, Nyengaard JR, Jespersen SN, Hansen B, 2016 Fast diffusion kurtosis imaging of fibrotic mouse kidneys. NMR Biomed. 1–11. 10.1002/nbm.3623.

Kunz N, da Silva AR, Jelescu IO, 2018 Intra- and extra-axonal diffusivities in the white matter: which one is faster? Neuroimage 181 10.1016/j.neuroimage.2018.07.020.

Le Bihan D, Brenton E, Lallemand D, Grenier P, Cabanis E, Laval-Jeantet M, 1986 MR imaging of intravoxel incoherent motions: application to diffusion and perfusion in neurological disorders. Radiol 161 (2), 401–407. 10.1148/radiology.161.2.3763909.

Le Bihan D, Urayama S-i., Aso T, Hanakawa T, Fukuyama H, 2006 Direct and fast detection of neuronal activation in the human brain with diffusion MRI. Proc. Natl. Acad. Sci. Unit. States Am. 103 (21), 8263–8268. 10.1073/pnas.0600644103.

Mitra P, Brownstone RM, 2012 An in vitro spinal cord slice preparation for recording from lumbar motoneurons of the adult mouse. J. Neurophysiol 107, 728–741. 10.1152/jn.00558.2011. [PubMed: 22031766]

Mori S, Crain BJ, Chacko VP, Van Zijl PCM, 1999 Three-dimensional tracking of axonal projections in the brain by magnetic resonance imaging. Ann. Neurol 45, 265–269. 10.1002/1531-8249(199902)45:2<265::AID-ANA21>3.0.CO;2-3. [PubMed: 9989633]

Oh S-H, Chung J-Y, In M-H, Zatsev M, Kim Y-B, Speck O, Cho Z-H, 2012 Distortion correction in EPI at ultra-high-field MRI using PSF mapping with optimal combination of shift detection dimension. Magn. Reson. Med 68, 1239–1246. 10.1002/mrm.23317. [PubMed: 22213517]

Roussel T, Frydman L, Le Bihan D, Ciobanu L, 2019 Brain sugar consumption during neuronal activation detected by CEST functional MRI at ultra-high magnetic fields. Sci. Rep 9, 4423 10.1038/s41598-019-40986-9. [PubMed: 30872689]

Schilling K, Gao Y, Janve V, Stepniewska I, Landman BA, Anderson AW, 2017 Can increased spatial resolution solve the crossing fiber problem for diffusion MRI? NMR Biomed. 10.1002/nbm.3787.

Shepherd TM, Ozarslan E, Yachnis AT, King MA, Blackband SJ, 2007 Diffusion tensor microscopy indicates the cytoarchitectural basis for diffusion anisotropy in the human hippocampus. AJNR Am. J. Neuroradiol. 28 (5), 958–964. [PubMed: 17494678]

Springer CS Jr., 2018 Using 1H2O MR to measure and map sodium pump activity in vivo. J. Magn. Reson 291, 110–126. 10.1016/j.jmr.2018.02.018. [PubMed: 29705043]

Stanisz GJ, 2003 Diffusion MR in biological systems: tissue compartments and exchange. Isr. J. Chem 43, 33–44. 10.1560/E0WU-7FFH-31M6-VLYT.

Tasaki I, Iwasa K, 1981 Rapid mechanical changes in crab nerve and squid axon during action potentials. J. Physiol 77 (9), 1055–1059.

Teorell T, 1962 Excitability phenomena in artificial membranes. Biophys. J 2 (2), 27–52. [PubMed: 14039678]

Veraart J, Poot DHJ, Van Hecke W, Blockx I, Van der Linden A, Verhoye M, Sijbers J, 2011 More accurate estimation of diffusion tensor parameters using diffusion kurtosis imaging. Magn. Reson. Med 65 (1), 138–145. 10.1002/mrm.22603. [PubMed: 20878760]

Zhang Y, Poirier-Quinot M, Springer CS Jr., Balschi JA, 2011 Active trans-plasma membrane water cycling in yeast is revealed by NMR. Biophys. J 101, 2833–2842. 10.1016/j.bpj.2011.10.035. [PubMed: 22261073]

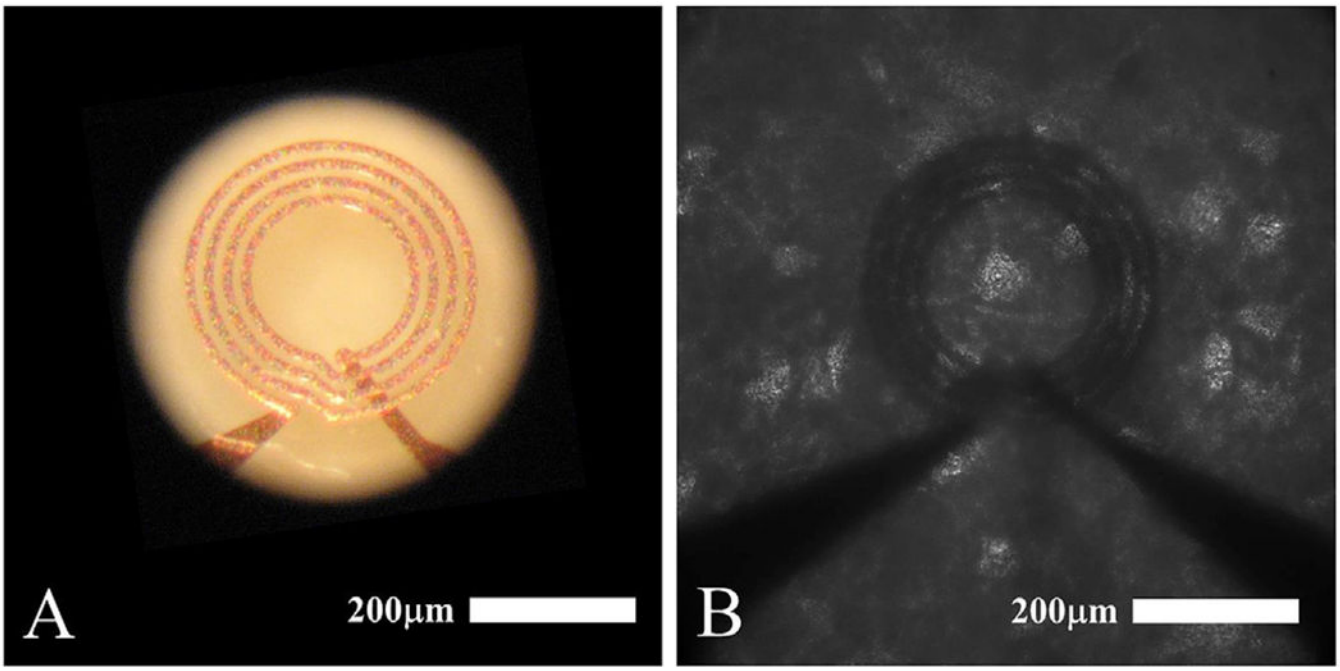

Fig. 1.

Tissue slice positioning in the 200 μm diameter, 4-turn micro surface coil. (A) A color image of the specialized, micro surface coil employed in our MR microscopy studies as seen through a dissecting scope. (B) Black and white image of a spinal cord slice overlaid on the RF coil during tissue placement. The perikaryon of an α-motor neuron is clearly visible centered within the coil's interior diameter.

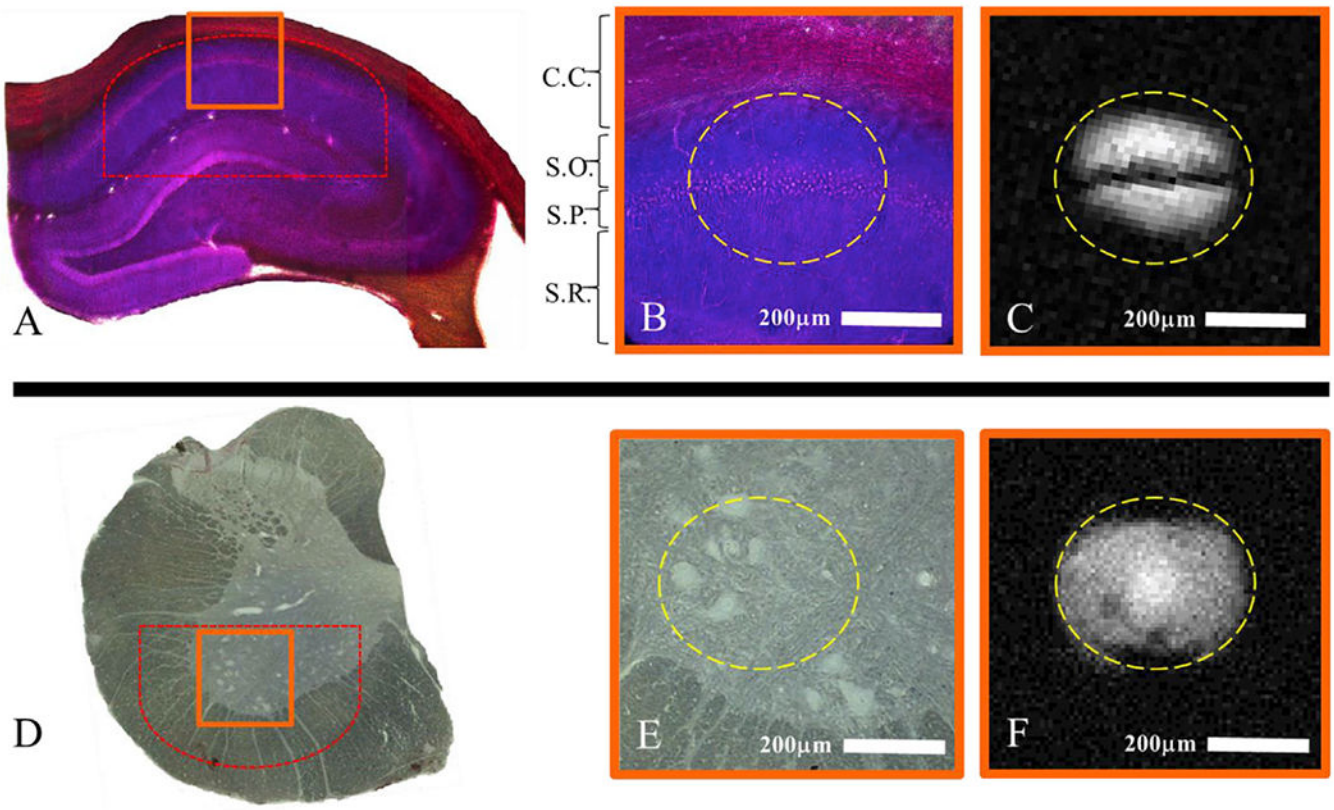

Fig. 2.

Diffusion-weighted MRM in the hippocampus and spinal cord. (A) Nissl-stained cross section of the rat hippocampus detailing the tissue regions employed in our perturbation studies. The boundary of the excised sample region employed in the activation experiments is indicated (red dashed line) as are the exterior dimensions of the corresponding histology and MR microscopy images (orange box). (B) Higher magnification of the inset from panel (A) detailing the lamina within the CA1 region: C.C. = corpus callosum, S.O. = stratum oriens, S.P. = stratum pyramidale, S.R. = stratum radiatum. The dimensions of the tissue region excited by the micro surface coil is indicated (dashed yellow line). (C) A representative, diffusion-weighted MR microscopy image of tissue lamina in the CA1 region of an acute hippocampal slice. (D) An unstained, transverse spinal cord slice from the lumbar enlargement bisected along the axis shared by the dorsal median septum and ventral median fissure. The boundary of the excised sample region employed in the kainate exposure experiments is indicated (red dashed line) as are the exterior dimensions of the corresponding histology and MR microscopy images (orange box). (E) Higher magnification of the inset from panel (D) detailing multiple α-motor-neuron cell bodies within the ventral horn as well as the boundary between gray and white matter regions. The dimensions of the tissue region excited by the micro surface coil is indicated (dashed yellow line). (F) A representative, diffusion-weighted MR microscopy image of α-motor cell bodies in an acute spinal cord slice. Note: Histology and MR images in this figure are comparative rather than correlative and are thus only for illustrating the gross anatomical features of the tissues under investigation. Kainate exposure (100 μM) was performed on living, acute slices

undergoing superfusion while histology images were conducted on a separate set of formaldehyde-fixed tissue sections.

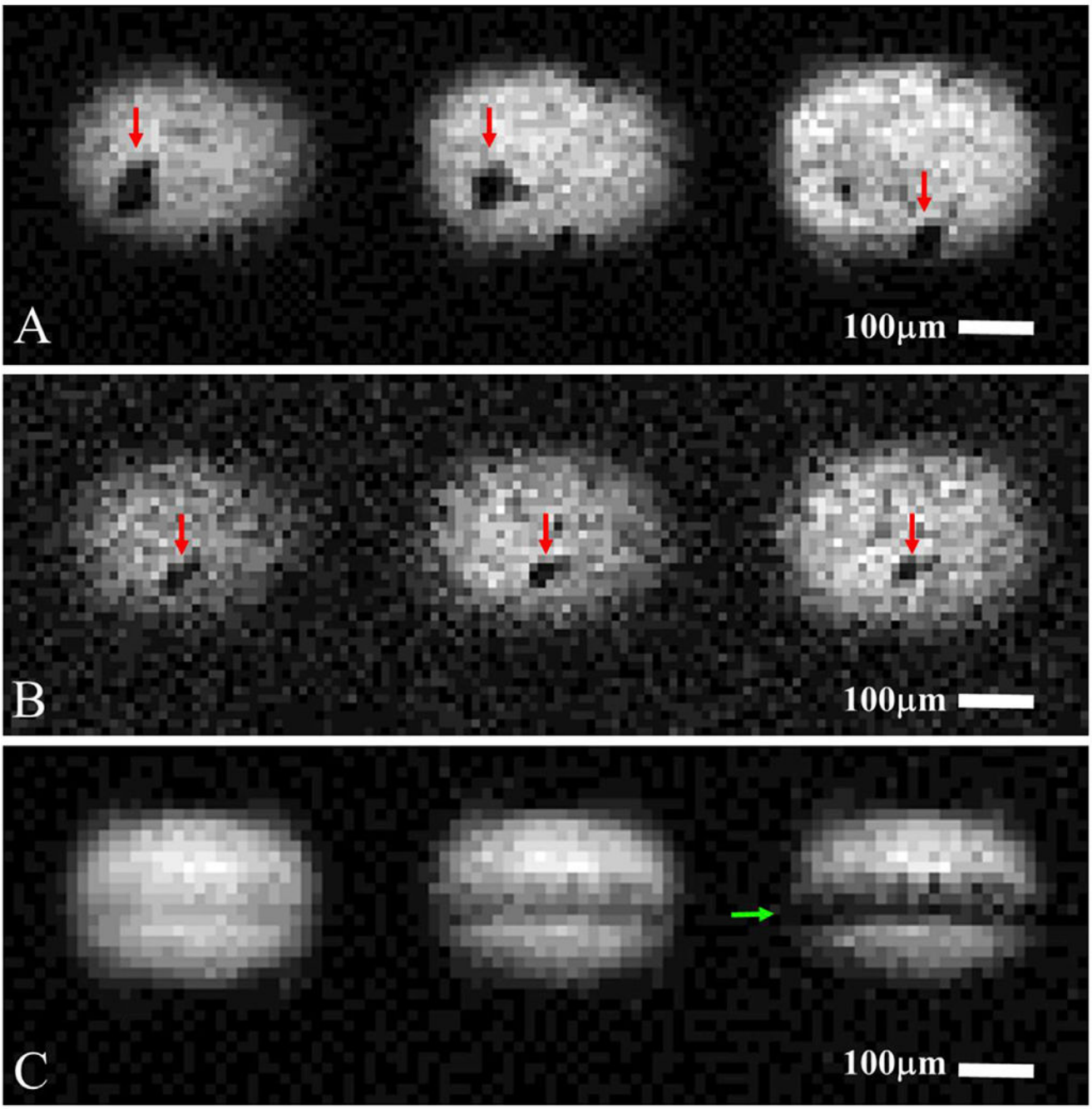

Fig. 3.

MR microscopy of living mammalian cells. (A & B) Top and middle rows contain three sequential frames taken at isotropic resolution (11 x 11 × 11 μm) from two different 3D, diffusion weighted (b effective = 1900 s/mm^2) MR microscopy experiments. These collections were performed on live, acute spinal cord slices (200 μm thick) taken from the lumbar enlargements of rats. The top series (A, SNR = 36.7) was generated using a much longer collection (9 h 6 min) to maximize signal intensity while the middle row (B, SNR = 11.8) was taken in an effort to optimize collection time (2 h 16 min). (C) Montage depicting

the CA1 region of the live hippocampus (16 x 16 × 200μm) taken at three diffusion weightings that increase left to right (b effective = 600, 1300, 3600 s/mm^2; SNR = 50.0, 33.3, 19.3). Despite the differences in collection parameters, perikarya of α-motor neurons (red arrows) and the stratum pyramidale containing the closely packed cell bodies of pyramidal neurons (green arrow) are visible in each series. Interestingly, the diffusion contrast properties seen in these examples collected on living slices—dark cellular interior surrounded by brighter areas of adjacent neuropil—are the same as those reported previously in experiments employing aldehyde-fixed tissue sections.

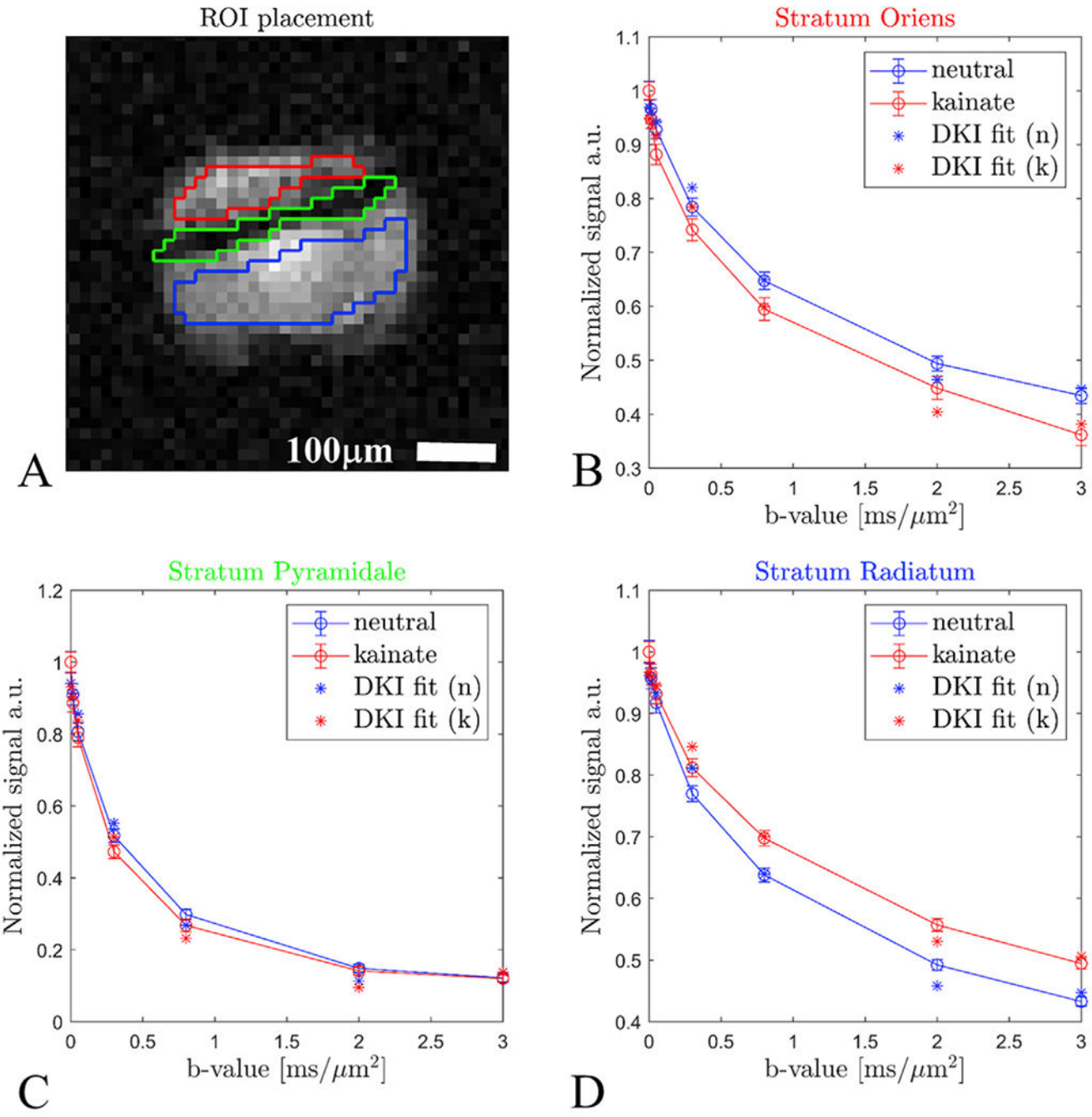

Fig. 4.

Detection of chemically driven (100 μM kainate) diffusivity changes in living cells. (A) Representative diffusion weighted (b effective = 4800 s/mm^2), MR microscopy image taken in the CA1 region of an accute hippocampal slice overlaid with regions of interest (ROI) selections for the strata oriens (red), pyramidale (green), and radiatum (blue). (B, C, & D) Diffusion signal decay curves compiled from each tissue type within the CA1 region during pre (blue curves) and post (red curves) exposure intervals. Upon exposure to kainate, diffusivity increases slightly (p = 0.081) in the pyramidale cell layer (C) while it increases

significantly ($p = 0.045$) in the stratum oriens (B) and decreases ($p = 0.076$) in the stratum radiatum (D). Thus, changes in the ADC reported in the strata radiatum and pyramidale were only at trend level. This diffusivity behavior was typical of all perturbation experiments conducted in the hippocampus. Diffusion signal measurements in the spinal cord were taken across the entire image field of view and thus ROIs were comprised of parenchyma within the ventral horn. Error bars in panels B through D represent standard error of the mean.

Table 1

Summary of results from our diffusion kurtosis imaging (DKI) experiments conducted before and after kainate exposure (100 μM kainate) in acute hippocampal (n = 8) and spinal cord (n = 5) slices. Tissues reported include the strata oriens, pyramidale and radiatum of the rat hippocampus and the ventral horn gray matter within the lumbar enlargement of the rat spinal cord. Groups which displayed significantly different diffusion properties following exposure to 100 μM kainate are marked with an asterisk. Results are presented as group mean ± the standard error of the mean.

Tissue and Condition	Mean Apparent Diffusion ($\mu m^2/ms$)	Mean Apparent Kurtosis
Oriens (Pre Kainate)	0.378 ± 0.043	1.674 ± 0.107
Oriens (Post Kainate)	0.428 ± 0.055 *	1.609 ± 0.144
Pyramidale (Pre Kainate)	0.993 ± 0.148	0.690 ± 0.056
Pyramidale (Post Kainate)	1.065 ± 0.173	0.778 ± 0.066
Radiatum (Pre Kainate)	0.412 ± 0.033	1.965 ± 0.072
Radiatum (Post Kainate)	0.373 ± 0.025	2.007 ± 0.095
Ventral Horn (Pre Kainate)	0.213 ± 0.009	1.280 ± 0.168
Ventral Horn (Post Kainate)	0.183 ± 0.010 *	1.001 ± 0.2204